

1 **Title**

2 A Spike Trimer Dimer-Inducing Nanobody with Anti-Sarbecovirus Activity

3 **Authors**

4 Iris C. Swart^{1,2}, Oliver J. Debski-Antoniak², Aneta Zegar³, Thijs de Bouter², Marianthi Chatziandreou²,

5 Max van den Berg¹, Ieva Drulyte⁴, Krzysztof Pyrć³, Cornelis A.M. de Haan², Daniel L. Hurdiss², Berend-

6 Jan Bosch², Sabrina Oliveira^{1,5}

7 ¹Cell Biology, Neurobiology and Biophysics, Department of Biology, Science Faculty, Utrecht University,
8 Utrecht, The Netherlands.

9 ²Virology section, Division of Infectious Diseases and Immunology, Department of Biomolecular Health
10 Sciences, Faculty of Veterinary Medicine, Utrecht University, Utrecht, The Netherlands.

11 ³Laboratory of Virology, Malopolska Centre of Biotechnology, Jagiellonian University, Krakow, Poland

12 ⁴Materials and Structural Analysis, Thermo Fisher Scientific, Eindhoven, The Netherlands

13 ⁵Pharmaceutics, Department of Pharmaceutical Sciences, Faculty of Science, Utrecht University, Utrecht, The
14 Netherlands.

15

16 **Corresponding author**

17 Correspondence to Sabrina Oliveira, s.oliveira@uu.nl

18

19 **Abstract**

20 The continued emergence and zoonotic threat posed by coronaviruses highlight the urgent need for
21 effective antiviral strategies with broad reactivity to counter new emerging strains. Nanobodies (or
22 single-domain antibodies) are promising alternatives to traditional monoclonal antibodies, due to
23 their small size, cost-effectiveness and ease of bioengineering. Here, we describe 7F, a llama-derived
24 nanobody, targeting the spike receptor binding domain of sarbecoviruses and SARS-like
25 coronaviruses. 7F demonstrates potent neutralization against SARS-CoV-2 and cross-neutralizing
26 activity against SARS-CoV and SARS-like CoV WIV16 pseudoviruses. Structural analysis reveals 7F's
27 ability to induce the formation of spike trimer dimers by engaging with two SARS-CoV-2 spike RBDs,
28 targeting the highly conserved class IV region. Bivalent 7F constructs substantially enhance
29 neutralization potency and breadth, up to more recent SARS-CoV-2 variants of concern. Furthermore,
30 we demonstrate the therapeutic potential of 7F against SARS-CoV-2 in the fully differentiated 3D
31 tissue cultures mirroring the epithelium of the human airway *ex vivo*. The broad sarbecovirus activity
32 and distinctive structural features of 7F underscore its potential as promising antiviral against
33 emerging and evolving sarbecoviruses.

34 **Introduction**

35 In recent years, two severe acute respiratory syndrome (SARS)-related coronaviruses (SARS-CoVs)
36 have crossed over from zoonotic reservoirs to humans, causing the SARS-CoV epidemic in 2003 and
37 the SARS-CoV-2 pandemic declared in 2020 (1,2). Both SARS-CoV-2 and SARS-CoV belong to the
38 subgenus *Sarbecovirus* within the genus *Betacoronavirus*, which otherwise comprises a large variety
39 of SARS-like coronaviruses that circulate mainly in bats, including high-risk strains such as RaTG13,
40 WIV1, SARS-like CoV WIV16 and RsSHC014 (2–4). Given the potential for new zoonotic spillover events
41 of viruses within this subgenus, there is an urgent need for broad-spectrum therapeutics capable of
42 targeting conserved epitopes across the subgenus *Sarbecovirus*. SARS-CoV-2 and SARS-CoV utilize the
43 angiotensin-converting enzyme 2 (ACE2) as their entry receptor, which they engage via the receptor-
44 binding domain (RBD) present within the spike (S) glycoprotein (2,5,6). In its prefusion state, the spike
45 protein forms a homotrimer and undergoes significant structural changes to regulate the exposure
46 and availability of the RBD. This occurs through an alternating "up" and "down" mechanism, wherein
47 the RBD transitions between a state that is accessible to receptors (in the "up" conformation) and a
48 state that is not accessible to receptors (in the "down" conformation) (7,8). The RBD has become a
49 main target for therapeutic development. During the SARS-CoV-2 pandemic, research on nanobodies
50 gained momentum alongside traditional monoclonal antibody (mAb) approaches (9).

51 Nanobodies, also known as single-domain antibodies (sdAbs) or VHJs (Variable Heavy domain of
52 Heavy chain antibodies), constitute the variable domain of heavy-chain antibodies found in, amongst
53 others, camelids and cartilaginous fishes (10–12). These small binding fragments of approximately 15
54 kDa, are extremely stable, can facilitate excellent tissue penetration and can easily be bio-engineered
55 into multivalent formats (13–15). In contrast to conventional antibodies, nanobodies can be produced
56 at low-cost in bacterial systems and their high stability and small size allows for intranasal
57 administration (16). For respiratory pathogens, like sarbecoviruses, intranasal delivery is preferred for
58 localized high concentrations, faster onset, and reduced systemic exposure (17). These attributes
59 combined make nanobodies highly valuable for engineering innovative biotherapeutics with potent
60 and broad antiviral activity against viral pathogens.

61 Targeting conserved epitopes on the CoV S, particularly within the RBD, offers multiple advantages:
62 broad coverage across various sarbecovirus strains, heightened resistance to neutralization escape,
63 and the potential to counteract future emerging strains. Notably, several nanobodies with broad
64 sarbecovirus activity have been described, of which the majority targets the RBD (18–25). Two
65 conserved epitopes on the spike RBD have been well characterized, the class III and IV epitopes, as
66 classified by Barnes et al., (26–28). Multiple class IV antibodies, broadly targeting sarbecoviruses have

67 been identified and characterized during the pandemic (29–33). The occluded nature of the class IV
68 epitope likely contributes to its conserved characteristics amongst the sarbecoviruses.

69 Here, we present a novel class IV epitope nanobody, 7F, with broad neutralization activity towards
70 sarbecoviruses. We structurally characterized the spike binding mode of this nanobody and evaluated
71 its neutralization potency and breadth. The binding of 7F allows simultaneous interaction with the
72 RBDs of two spike proteins, inducing S-ectodomain trimer dimers - a phenomenon which has only
73 been reported previously twice (24,34). Additionally, we evaluated the neutralization potency and
74 breadth of 7F after dimerization. The combination of targeting a conserved epitope and displaying
75 broad reactivity towards sarbecoviruses, positions 7F as a promising candidate for combating future
76 outbreaks.

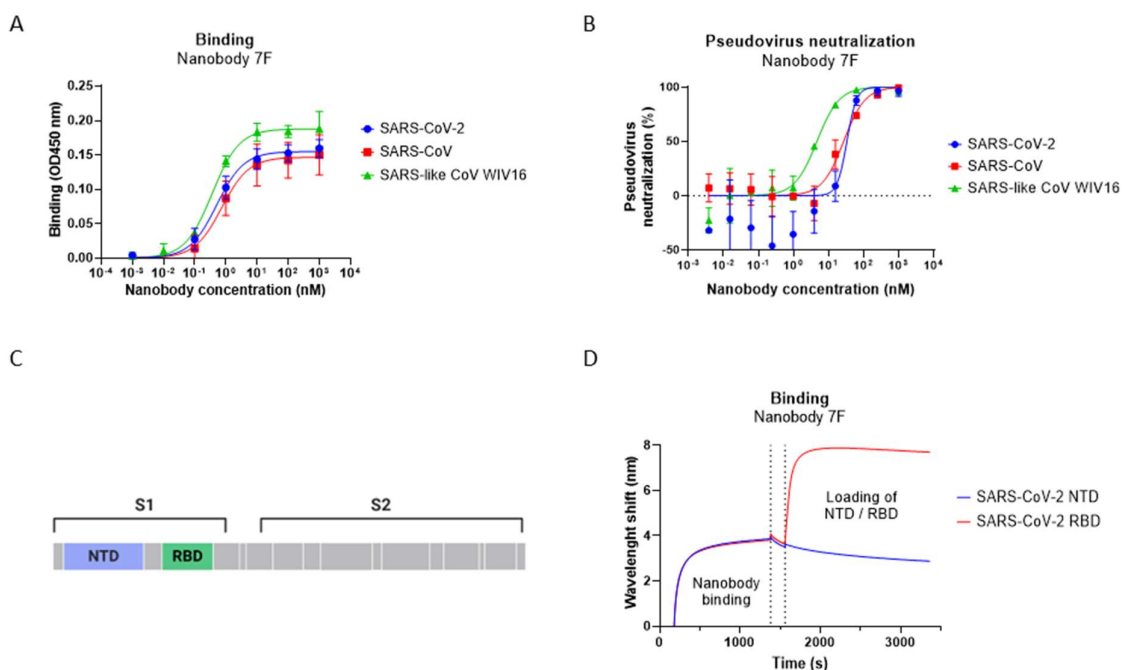
77

78 **Results**

79 **Identification of broadly reactive sarbecovirus targeting nanobody 7F**

80 To elicit an immune response and isolate sarbecovirus S-targeting nanobodies, two llamas were
81 immunized with prefusion trimeric spike proteins of multiple betacoronaviruses, including SARS-CoV
82 and SARS-CoV-2. Thereafter, blood was collected and phagemid libraries were generated and pooled
83 for the nanobody selection process. Two consecutive rounds of phage panning against SARS-CoV-2
84 RBD, followed by phage ELISAs, resulted in five unique sequences of promising nanobody candidates.
85 Further characterization of the purified monovalent nanobodies revealed their high-affinity binding to
86 the SARS-CoV-2 spike protein and their capacity to neutralize SARS-CoV-2 pseudovirus (**Fig. S1A-B**).
87 Given the study's focus on developing broad neutralizing sarbecovirus nanobodies, we evaluated their
88 cross-reactivity to SARS-CoV and SARS-like CoV WIV16. Notably, two of the selected nanobodies,
89 namely nanobody 7F and 9A, demonstrated binding to SARS-CoV and SARS-like CoV WIV16 as well
90 (**Fig. S1C**). Furthermore, both nanobodies were capable of cross-neutralization of SARS-like CoV WIV16
91 pseudovirus (**Fig. S1D**).

92 Of the two cross-reactive nanobody candidates, 7F was selected for further analysis, as it exhibited
93 low nanomolar (nM) binding affinity to all three sarbecoviruses in ELISA (**Fig. 1A**) and demonstrated
94 broad neutralization activity against pseudoviruses of SARS-CoV-2, SARS-CoV and SARS-like CoV
95 WIV16, with IC_{50} values falling in the nM range (33.4 \pm 17.2, 27 \pm 5 and 4.7 \pm 0.9 nM respectively; **Fig.**
96 **1B**). To evaluate the epitope location of 7F on the spike protein, biolayer interferometry (BLI) was
97 performed. The strong binding signal of 7F to the spike RBD in contrast to the spike protein N-terminal
98 domain (NTD) reveals that 7F binds to an epitope on the RBD (**Fig. 1C-D**).



99

100 **Figure 11 Camelid-derived nanobody 7F shows cross-reactivity activity against sarbecoviruses. A. ELISA-based**
101 **reactivity of 7F to plate-immobilized spike ectodomain of SARS-CoV-2, SARS-CoV and RBD of SARS-like-CoV**
102 **WIV16. Data points represent the mean \pm SDM of $n = 3$ replicates from one representative of three independent**
103 **experiments. B. Neutralization of SARS-CoV-2, SARS-CoV and SARS-like CoV WIV16 pseudovirus by serial diluted**
104 **nanobody on VeroE6 cells. Data points represent the mean \pm SDM of $n = 3$ replicates from one representative of**
105 **two independent experiments. C. Schematic representation of the SARS-CoV-2 spike protein, with NTD and RBD**
106 **labeled D. Binding of 7F to different spike domains analyzed by BLI. 7F was immobilized on NTA sensors, after**
107 **which 7F was saturated in binding with either SARS-CoV-2 NTD or RBD. Data shown is based on a single**
108 **experiment.**

109

110 7F induces formation of SARS-CoV-2 spike trimer dimers

111 To gain insight into the interaction site of 7F, cryo-electron microscopy (cryo-EM) single particle
112 analysis was performed on the prefusion-stabilized SARS-CoV-2 ancestral Wuhan spike ectodomain
113 trimer complexed with 7F (Fig.2). Two-dimensional classification analysis revealed only particles
114 representing a head-to head spike trimer dimer (Fig.S2A). Three-dimensional classification further
115 confirmed this phenomenon, with a single class representing a trimer dimer observed. All six RBDs are
116 in the “up” conformation and subsequently interact with six molecules of 7F (Fig.2A-C). Further
117 processing yielded a final reconstruction with a global resolution of 3.3 Å (Fig.S2-3). Local refinement
118 improved the resolution at the interface to 3.1 Å (Fig.2A + B and Fig.S2-3), allowing accurate modelling
119 and characterization of the interacting residues at the 7F-RBD interfaces.

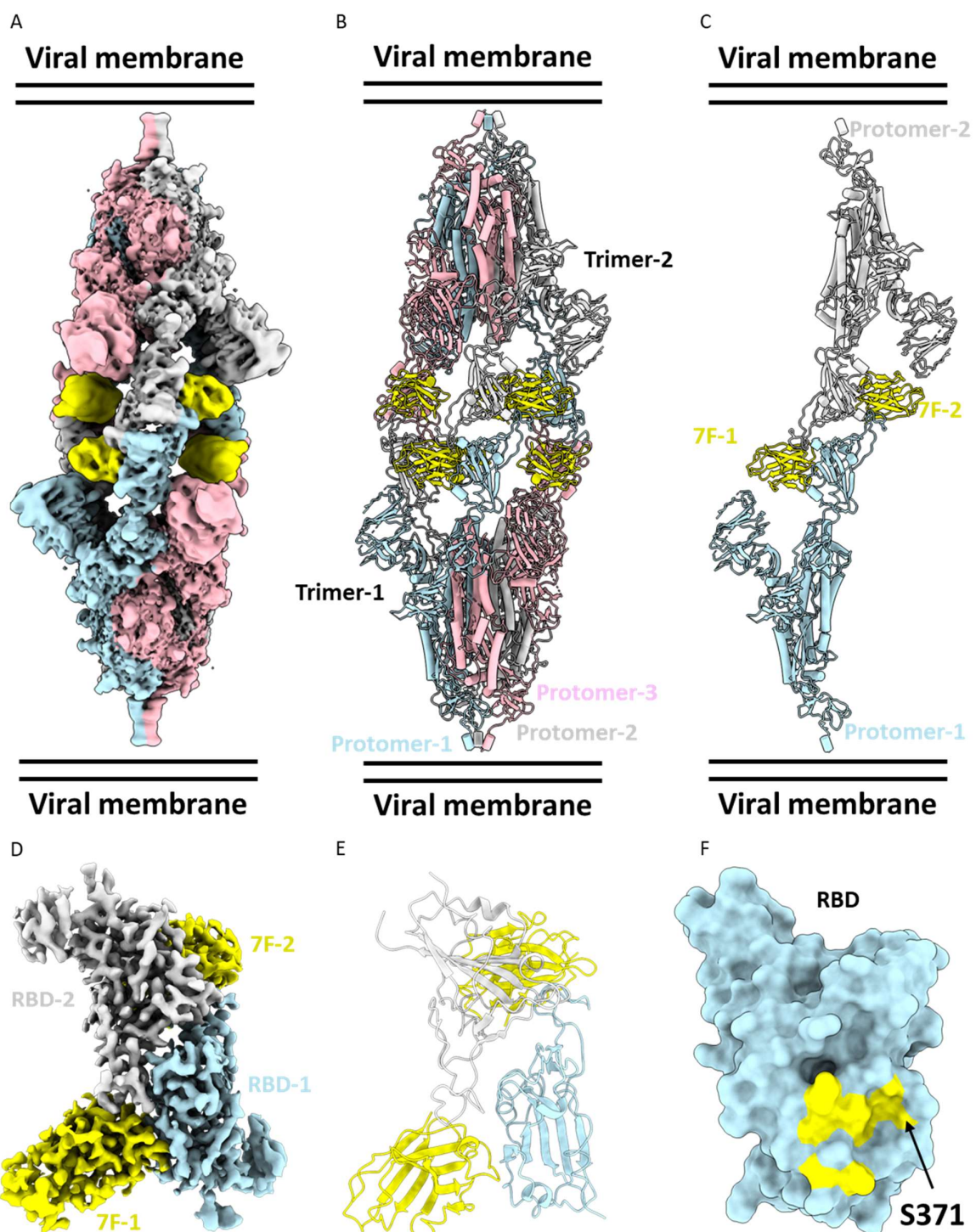
120 The 7F-RBD complex contains three binding interfaces. Two of these interfaces are between the
121 juxtaposed RBDs and a 7F molecule, labelled as ‘interface-major’ and ‘interface-minor’ based on the
122 surface area buried in each RBD-7F interaction. While the third interface is between opposing RBDs
123 and labelled “RBD-RBD-interface”. Interface-major constitutes a buried surface area of 638 Å² and is
124 likely solely responsible for the single dominant binding affinity measured in ELISA assays (**Fig. 1A**). The
125 interface-minor consists of a buried surface area of 165 Å², predominantly involving residues in the
126 CDR3 loop, but also a single residue from framework-2 of 7F. Surprisingly, the proximity in which the
127 interaction between RBDs and 7Fs in the dimer formation takes place, allowing for a third interaction
128 between both RBDs. This “RBD-RBD” interface creates a further buried surface area of 1008 Å²
129 between the receptor binding motif of each RBD.

130 The interface-major interaction coincides with that of class IV anti-RBD mAbs (**Fig. 2C**). To understand
131 this major interaction, we compared a range of both antibodies and nanobodies from class IV (**Fig. S4**).
132 Monoclonal antibodies such as S2X259 (30), EY6A (32), CR-3022 (29), S304 (31) and nanobody VHH72
133 (25) largely overlap the binding surface of 7F, while the monoclonal antibodies H014 (33) and S2A4
134 (31) encompass the entirety of the 7F interface-major binding surface. These antibodies and
135 nanobodies exclusively bind SARS-CoV-2 RBD in an “up” conformation, but do not induce trimer dimer
136 formation. It is likely that the interactions observed here at site Interface-minor drive the dimerization
137 resulting in the RBD-RBD interface, through shape-complementation.

138 The antibody cluster S2A4, EY6A, CR3022 and S304 have been shown to be capable of triggering S1
139 shedding by Cryo-EM (31,32,35). The binding sites for these antibodies are completely buried in the
140 spike ectodomain when RBD is in the “down” conformation, with at least a “2-up” RBD conformation
141 required for interaction, due to clashes of the Fab fragments with the adjacent “down” RBD, S2 subunit
142 and NTDs (32,35). In the context of the closed S, the 7F binding site is occluded. Superimposition of 7F
143 to “1-up” and “2-up” SARS-CoV-2 S-ectodomains, suggest only a “3-up” conformation would allow
144 binding (**Fig. S5**), due to clashes with adjacent RBD, NTD and S2 subunits, like those observed in Fab
145 fragment interactions of the above antibodies. We did not observe S1 shedding here, via Cryo-EM,
146 likely due to the proline substitutions (6P) and a mutated furin cleavage site incorporated into our S-
147 ectodomain construct to stabilize the prefusion conformation of the spike (36).

148 Binding of the spike trimer to the ACE2 receptor extends the RBDs outwards resulting in S1 shedding,
149 which ultimately allows viral entry (8). The afore antibodies have been shown to act as ‘molecular
150 ratchets’, biasing the SARS-CoV-2 spike conformational equilibrium toward opened RBDs, resulting in
151 rotation beyond 20°, and hyperextension outwards to various extents, in order to accommodate Fab
152 fragment binding. Subsequently, this causes the premature release of the S₁ subunit. MAb S2A4

153 (PDB:7JVC) (31), wrenches the RBD, resulting in a 48° rotation and a 15 Å hyperextension, when
154 compared to ACE2-bound spike-ectodomain (PDB:7A98) (8) (**Fig. S6**). For the 7F-RBD complex, we
155 observe a 55° rotation of the RBD and an 8 Å hyperextension compared to the ACE2-bound spike-
156 ectodomain (**Fig. S6**). The similarities in conformations we have found between the 7F-complex and
157 previously published structures where S1 shedding is induced, suggest 7F exerts its antiviral activity
158 through a similar mechanism.

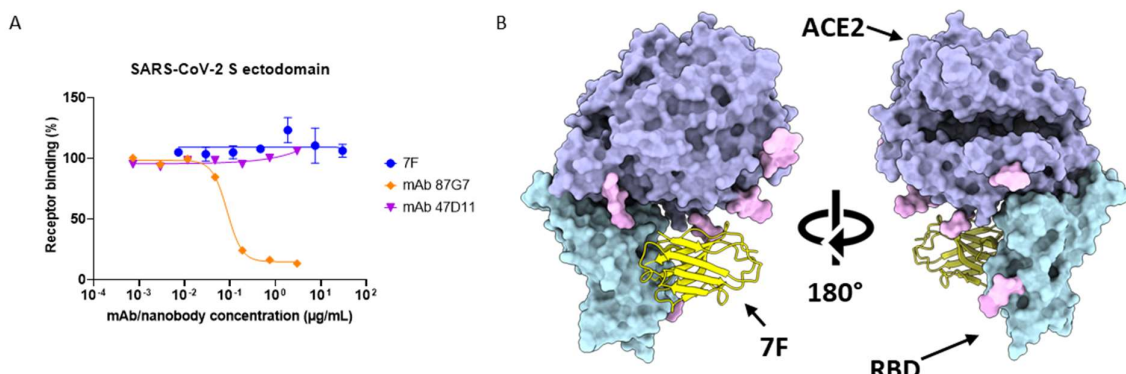


160 **Figure 2 Structural analysis of 7F in complex with the SARS-CoV-2 spike trimer.** **A.** EM density map. The complex
161 comprises six 7F molecules bound to two SARS-CoV-2 spike trimeric ectodomains. **B.** Atomic model of the six 7F
162 molecules bound to two SARS-CoV-2 spike trimeric ectodomains. Spike protein protomers are in blue, grey, and
163 pink, respectively. The 7F molecules are in yellow. **C.** Atomic model of a single protomer of each spike trimer,
164 bound to two 7F molecules. Protomer-1 is blue, protomer-2 is grey and both 7F molecules are represented in
165 yellow. **D.** Locally refined EM density map of the interaction site between two 7F molecules and two SARS-CoV-2
166 RBDs. **E.** Atomic model of the interaction site. RBD-1 is blue, RBD-2 is grey and 7F molecules are represented in
167 yellow. **F.** Surface representation atomic model of SARS-CoV-2 RBD (blue) with the 7F epitope highlighted
168 (yellow).

169

170 **7F does not interfere with the RBD-ACE2 interaction**

171 To understand the mechanism of virus neutralization, we assessed the possible interference of 7F with
172 S-mediated receptor-binding activity. An ELISA-based receptor binding inhibition assay revealed that
173 7F does not block the binding of SARS-CoV-2 spike ectodomain to the human ACE2 receptor (**Fig. 3A**).
174 Structural alignment of an ACE2 RBD structure (PDB: 6VW1) (37) with a single molecule of 7F and
175 single RBD showed that the interaction 'major-interface' would not hinder ACE2 access to the spike
176 RBD (**Fig. 3B**). These results further suggest, the major interface interaction is the main driving force
177 of 7F neutralization and trimer dimer formation may be a phenomenon observed at the higher
178 concentrations of 7F and S-ecto used in our cryo-EM experiments.



179

180 **Figure 3 Functional and structural exploration of role of 7F in spike ACE2 interaction** **A.** ELISA-based receptor
181 binding inhibition assay. SARS-CoV-2 spike ectodomain preincubated with serially diluted 7F or control mAbs
182 87G7 (ACE2 binding competitor) and 47D11 (not competing with ACE2 binding), were added to a plate coated
183 with soluble human ACE2. The spike-ACE2 interaction was quantified using HRP-conjugated antibody targeting
184 the C-terminal Strep-tag fused to SARS-CoV-2 spike ectodomain. Data points represent the mean \pm SDM of $n = 3$
185 replicates from one representative of three independent experiments. Concentration displayed in µg/mL

186 corresponds to range of 0.001 – 1000 nM. **B.** Superimposition of human ACE2/SARS-CoV-2 complex (PDB: 6VW1
187 locally refined model of SARS-CoV-2 RBD-7F complex protein structure.

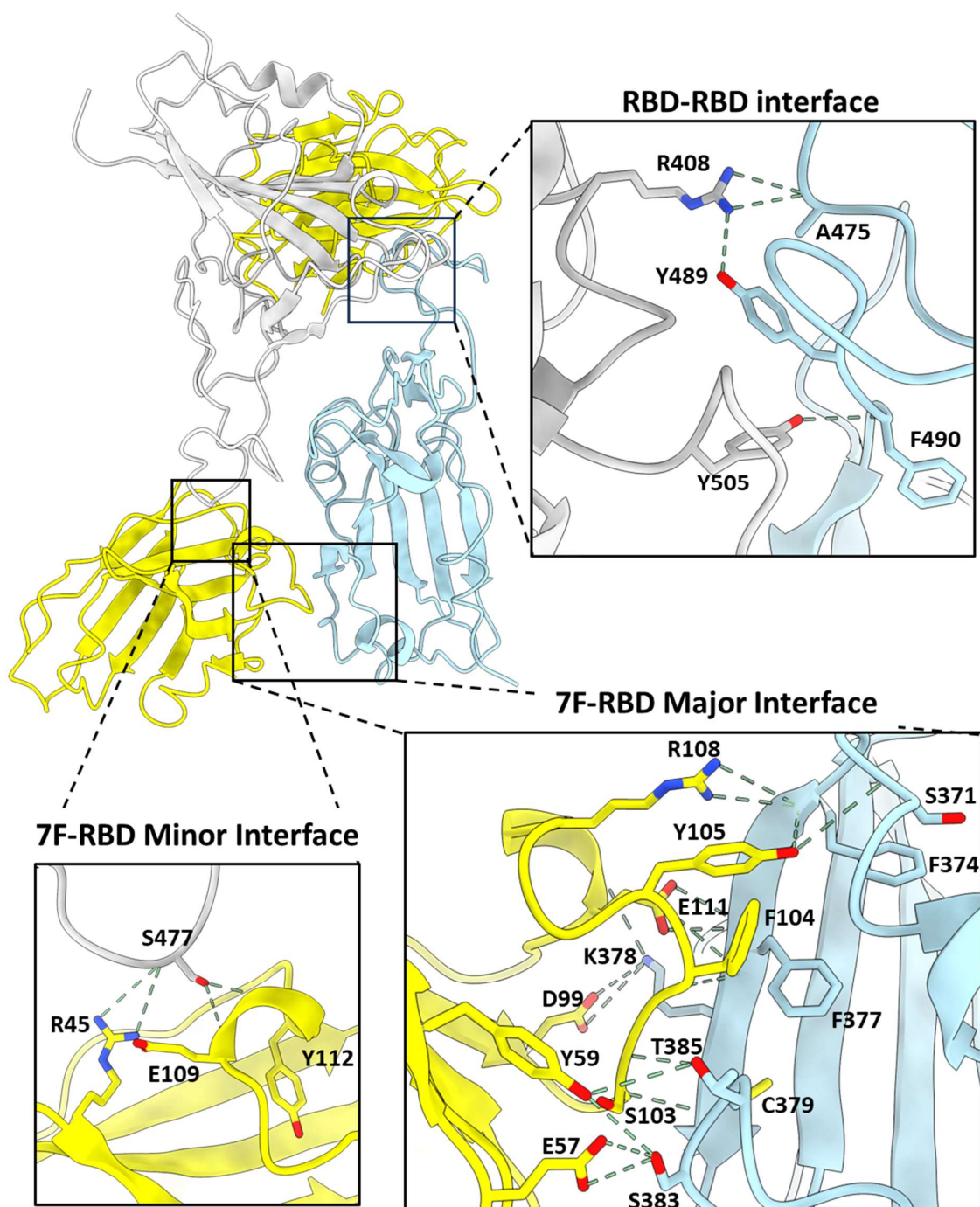
188

189 **Cryo-EM reveals the interactions of 7F with the RBD**

190 The major interface between 7F and the spike protein is characterized by a single salt bridge
191 connecting D99 of 7F and K378 of RBD, along with eight hydrogen bonds (Fig. 4). The extensive
192 interactions occur mainly through the long CDR3 loop of 7F, forming hydrogen bonds between D99,
193 S102, F104, Y105, R108, E111, and consecutive residues of the RBD beta strand S371-T379.
194 Additionally, two hydrogen bonds of the CDR2 loop, E57 and Y59, further stabilize the interaction with
195 residues S383 and T385 of the same beta strand.

196 On the other hand, the minor interface involves only three hydrogen bonds, each binding to a single
197 RBD amino acid S477 (Fig. 4). Interestingly, one of these interactions involves a residue, R45, from the
198 framework of 7F, while the other two residues are from the CDR3 loop. The close interactions of both
199 major and minor interfaces appear to facilitate the interaction between the RBD monomers, leading
200 to extensive hydrogen bonding between G404, R408, G485, Y489, F490, and Y505 of one RBD with
201 mirrored residues of the other RBD and resulting in a third interface, RBD-RBD.

202 While rare, trimer dimer formation has been induced by both mAb 6M6 (34) and nanobody Fu2 (24).
203 Additionally, the SARS-CoV-2 Kappa variant formed head-to-head trimer dimers without the
204 involvement of binding fragments (38). Although each of the binding molecules induces the formation
205 of distinct trimer dimers, they share some aspects of the interfaces formed with 7F-RBD interactions
206 described here (Fig. 4). The CDR3 of Fu2 similarly plays a predominant role in its major interface,
207 forming a salt bridge with K378, and additional hydrogen bonds with T376-Y380 of the RBD beta
208 strand, overlapping with residues reported here. Similarly, the formation of RBD-RBD interactions in
209 trimer dimers formed by mAb 6M6 involves similar residues and interfaces as 7F. One notable
210 difference between these molecules is that 7F-mediated trimer dimer formation is observed only with
211 the trimers of SARS-CoV-2 adopting a three-up RBD formation, whereas 6M6 and Fu2 form these
212 trimers with only two-up RBDs from different spike trimers of SARS-CoV-2.



213

214 *Figure 4 Structural basis for sdAb-7F binding to the SARS-CoV-2 RBD. Ribbon representation of the dimeric RBD-*
215 *7F complex, with inset panels showing detailed interactions for the major and minor interfaces.*

216

217

218

219 **Dimerization of 7F enhances neutralization potency**

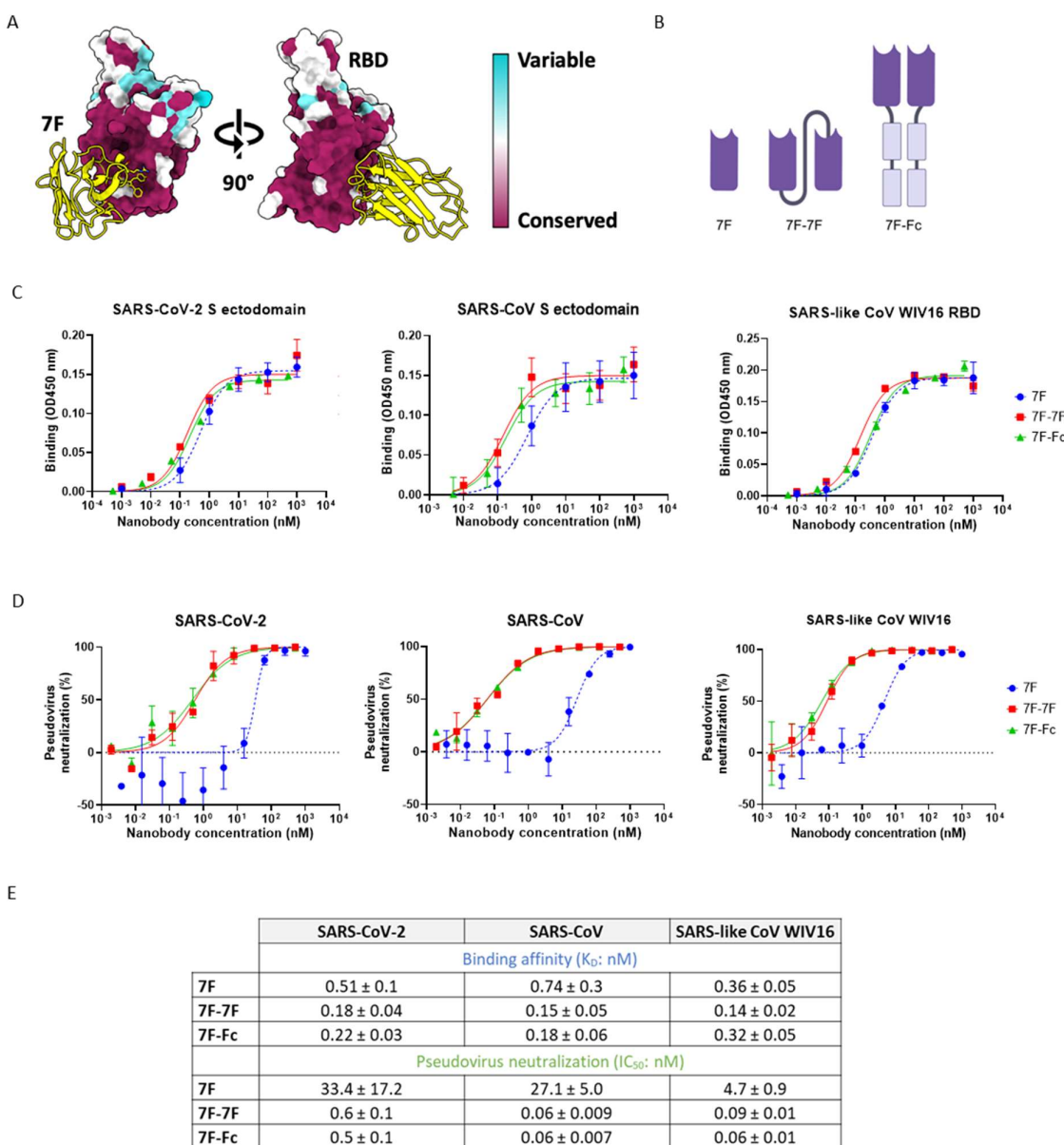
220 Since the major-interface of 7F is a class IV epitope of the SARS-CoV-2 RBD - a region of the RBD known
221 to be highly conserved amongst sarbecoviruses - we aimed to assess the conservation of the 7F
222 binding site within the subgenus *Sarbecovirus* (28). For this, we mapped conserved and variable
223 residues onto the RBD of the monomeric 7F-RBD complex (**Fig. 5A**). We found that all interacting
224 residues of the RBD showed high conservation across selected sarbecoviruses, suggesting that 7F may
225 exhibit binding and be able to neutralize many other sarbecoviruses and SARS-like CoVs, besides SARS-
226 CoV-2, SARS-CoV and SARS-like CoV WIV16 tested here.

227 Nanobody multimerization is known for its potential to enhance binding affinity, neutralization
228 efficacy, and restore loss of binding and neutralization potency due to the antigenic drift in SARS-CoV-
229 2, such as in [16,38]. Therefore, we engineered two distinct bivalent nanobody constructs. The first
230 leverages insights from the cryo-EM structure, facilitating precise structure guided design of a
231 genetically linked bivalent nanobody, 7F-7F. This construct features a glycine-serine linker of 10 amino
232 acids long, that should enable simultaneous binding of two nanobodies to the spike trimer dimer
233 complex. Complementing this structural approach, we developed a bivalent Fc-fused nanobody, 7F-
234 Fc (**Fig. 5B**). Correct assembly of the Fc-fused construct by interchain disulfide bonds was confirmed
235 by the higher molecular weight bands on the native gel, compared to the monomer based bands
236 confirmed in the SDS gel (**Fig. S7**).

237 To ensure a fair comparison between monovalent and bivalent nanobodies, the constructs were
238 evaluated based on their molar concentration, i.e. 7F (15 kDa), 7F-7F (30 kDa) and 7F-Fc (80 kDa). In
239 the ELISA based binding assays, all 7F constructs showed high affinity binding, with apparent K_D values
240 in the low nM range, to spike proteins of SARS-CoV and SARS-CoV-2 and RBD of SARS-like-CoV WIV16
241 (**Fig. 5C, E**). Despite these promising high binding affinities, only a very small benefit of the bivalent
242 constructs over monovalent 7F was observed (**Fig. 5C**). The lack of substantial improvement in
243 apparent binding affinities suggest this ELISA may not reflect the avidity effect expected to be
244 observed for the bivalent nanobodies. Similar to the observations made with the monovalent
245 nanobody, the bivalent 7F constructs exhibited no interference with the spike-ACE2 interaction (**Fig.**
246 **S8**).

247 In contrast to the small change in apparent binding affinities, a substantial increase in neutralization
248 potency was observed for both the 7F-7F and 7F-Fc against SARS-CoV-2, SARS-CoV and SARS-like CoV
249 WIV16 pseudoviruses (**Fig. 5D**). The increase in potency observed for the bivalent nanobodies ranged
250 from 50-450 times, depending on the strain tested (**Fig. 5E**). The enhanced neutralization observed

251 was comparable for both 7F-7F and 7F-Fc, neutralizing the tested sarbecovirus pseudoviruses with IC_{50}
 252 values in the sub nM range.



253

254 **Figure 5 Enhanced neutralization potency of bivalent 7F constructs** **A.** Mapping of sarbecovirus amino acid
 255 conservation onto the surface representation of SARS-CoV-2 RBD in complex with 7F. **B.** Design of different 7F
 256 constructs, from left to right: 7F monomer, genetically linked bivalent 7F-7F and 7F-Fc fusion **C.** ELISA binding
 257 curves showing nanobody binding to immobilized SARS-CoV-2 spike ectodomain (left panel), SARS-CoV spike
 258 ectodomain (middle panel) and SARS-like CoV WIV16 RBD (right panel). Data points represent the mean \pm SDM,
 259 for $n = 3$ replicates from one representative of three independent experiments **D.** Nanobody mediated
 260 neutralization of luciferase encoding VSV particles pseudotyped with spike proteins of (left panel to right panel)
 261 SARS-CoV-2, SARS-CoV and SARS-like CoV WIV16 on VeroE6 cells. Data points represent the mean \pm SDM, for $n =$

262 3 replicates from one representative of two independent experiments **E**. Table showing the ELISA-based apparent
263 binding affinities (K_D) and pseudovirus neutralization based IC_{50} values of the monovalent and bivalent 7F
264 constructs against SARS-CoV-2, SARS-CoV and SARS-like CoV WIV16 proteins or pseudoviruses, respectively. IC_{50}
265 and K_D values (\pm standard deviation) were calculated from the binding and neutralization curves displayed in **B**
266 and **C**, respectively.

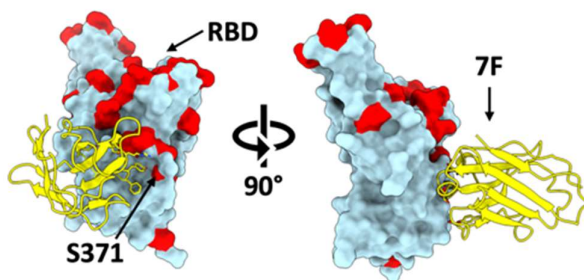
267

268 **Dimerization of 7F increases neutralization breadth against SARS-CoV-2 variants of concern**

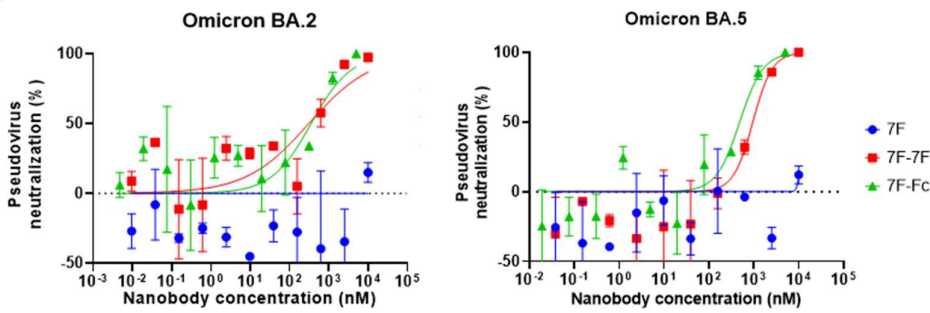
269 Structural insight into 7F's ability to inhibit SARS-CoV-2 variants of concern was gained by comparison
270 of interacting spike residues between these variants and 7F (**Fig. 6A**). Within 7F's major interface, we
271 observed a single mutation, S471L in Omicron BA.1, which further evolved to S471F in later variants
272 (**Fig. S9**). We anticipated that this mutation may abolish binding and/or neutralization of SARS-CoV-2
273 from Omicron and beyond. Consequently, we evaluated neutralization of our constructs against SARS-
274 CoV-2 Omicron BA.2 and BA.5 pseudoviruses. As anticipated, neither VOCs were neutralized by
275 monovalent 7F due to the 471 mutations. However, strikingly, in both bivalent forms, 7F recovered
276 neutralization activity against both Omicron BA.2 and BA.5 (**Fig 6B**), with IC_{50} values in the low
277 micromolar (μ M) range (**Fig. 6C**). This suggests that 7F, in the bivalent format, can overcome both
278 S471L and S471F mutations found in VOCs. Notably, both 7F-7F and 7F-Fc displayed comparable
279 neutralization potencies against these VOCs. It is reasonable to assume that the bivalent nanobody
280 constructs maintain neutralization potency against all VOCs included those most recent JN.1 and
281 BA.2.86, as these variants have not accumulated further mutations in the 7F interacting residues.
282 However, if the trimer dimer phenomenon does contribute to binding and neutralization of 7F, there
283 are further mutations which have been acquired in later VOCs in both the minor-interface and RBD-
284 RBD interface, which could hamper trimer dimer formation and therefore impact neutralization
285 potency (**Table S1**).

286

A



B



C

SARS-CoV-2 Omicron BA.2		SARS-CoV-2 Omicron BA.5	
Pseudovirus neutralization (IC_{50} : μM)			
7F	N.A.	N.A.	
7F-7F	0.31 ± 0.2	0.95 ± 0.4	
7F-Fc	0.35 ± 0.2	0.48 ± 0.2	

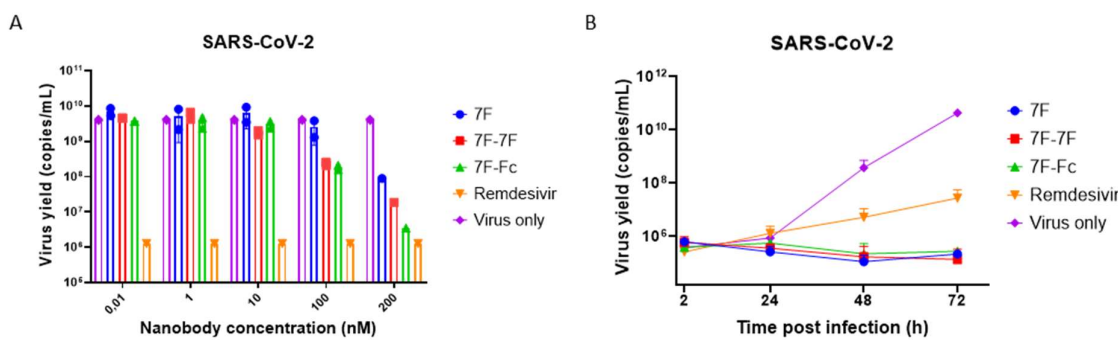
287

288 **Figure 6 Dimerization increases the neutralization breadth of 7F against SARS-CoV-2 variants-of-concern. A.**
289 *Mapping of SARS-CoV-2 amino acid conservation onto the surface of SARS-CoV-2 RBD in complex with 7F. B.*
290 *Nanobody mediated neutralization of luciferase encoding VSV particles pseudotyped with spike proteins of (left)*
291 *SARS-CoV-2 Omicron BA.2 and (right) SARS-CoV-2 Omicron BA.5 on VeroE6 cells. Data points represent the mean*
292 *\pm SDM, for $n = 3$ replicates from one representative of two independent experiments. C. Summary of the IC_{50}*
293 *values of the monovalent and bivalent 7F constructs against SARS-CoV-2 Omicron BA.2 and BA.5 pseudoviruses.*
294 *IC_{50} values (\pm standard deviation) were calculated from the neutralization curves displayed in B.*

295

296 **7F constructs effectively neutralize authentic SARS-CoV-2 infection in a fully differentiated 3D cell**
297 **model of the human airway epithelium**

298 We next investigated the neutralization potential of the 7F antibody formats against authentic SARS-
299 CoV-2 infection in A549^{ACE2+TMPRSS2+} cells. Consistent with the observations for SARS-CoV-2
300 pseudovirus, the bivalent nanobodies demonstrate increased potency compared to their monovalent
301 counterparts in neutralizing authentic SARS-CoV-2, with the IC₅₀ value improving 3-5 fold (Fig. 7A).
302 Furthermore, to explore the neutralization potency of the nanobodies in a more clinical relevant
303 setting, we utilized human air-liquid interface (ALI) cultures of primary human airway epithelium (HAE)
304 as an *ex vivo* model to replicate human infection. Our findings reveal that all three nanobody
305 constructs exhibited a potent response against authentic SARS-CoV-2 in HAE culture, with 100 nM of
306 nanobody being sufficient to completely inhibit infection over a 72 hour time period (Fig. 7B).
307 Interestingly, in contrast to our observation in the virus neutralization assay, 100 nM nanobody
308 surpassed the potency of 10 μM remdesivir against SARS-CoV-2 in the HAE culture.



309
310 **Figure 7 Monovalent and bivalent 7F constructs neutralize authentic SARS-CoV-2 in A549 cells and HAE cell**
311 **cultures. A.** Neutralization of SARS-CoV-2 in A549^{ACE2+TMPRSS2+} cells. Virus was pre-incubated with serial diluted
312 nanobody, or 10 μM remdesivir, for 30 min before infecting A549^{ACE2+TMPRSS2+} cells. Infection was quantified by
313 measuring the virus yield (viral RNA copies/ml, as determined with RT-qPCR) in cell culture supernatants of SARS-
314 CoV-2 infected cells. **B.** Neutralization of SARS-CoV-2 in HAE cell culture. HAE cultures were incubated with SARS-
315 CoV-2 and 100 nM nanobodies or 10 μM remdesivir on the apical side for 2 hours. Nanobody incubation was
316 repeated every 24 hours. Graph showing the quantification of viral replication in the cultures, evaluated by RT-
317 qPCR.

318 **Discussion**

319 In this study, we present a broadly reactive nanobody, 7F, that is targeting a conserved site in the
320 spike proteins of several sarbecoviruses. Through structural and functional analyses, we elucidated
321 7F's ability to achieve cross-neutralization of SARS-CoV-2, SARS-CoV, and SARS-like CoV WIV16
322 pseudoviruses. 7F targets a conserved class IV epitope on the spike RBD, facilitating neutralization
323 through a mechanism independent of receptor-binding inhibition. Our cryo-EM studies demonstrated
324 that 7F induces the formation of spike trimer-dimers, mediated by interactions with both major and
325 minor interfaces, on the spike RBD alongside a further RBD-RBD interface, likely induced by the
326 stabilization of the RBDs in a head-to-head configuration. Interestingly, these interactions not only
327 involve residues within the nanobody itself, but also highlight the role of RBD-RBD interactions in
328 forming these spike trimer dimers.

329 Alongside the SARS-CoV-2 Kappa variant, capable of forming spike trimer dimers independently (38),
330 CoV trimer-dimer formation has been reported previously for a nanobody and an antibody (24,34).
331 The full structural basis was explored for one of these trimer dimer forming nanobodies, Fu2.
332 Neutralization of Fu2 can partially be attributed to the aggregation of virions due to the trimer dimer
333 formation (24). This mechanism may provide an explanation for the improved neutralization by 7F,
334 though we could not validate this in our *in vitro* studies. While 7F-induced spike trimer-dimer
335 formation does not appear to be the driver of neutralization, our structure does provide insights into
336 nanobody induced higher order oligomerization, which could inform the design of new biparatopic
337 molecules in the future. Unlike some other class IV nanobodies, 7F does not impede the spike-ACE2
338 interaction, suggesting an alternative mode of action (19,25,40). Possibly 7F achieves neutralization
339 by destabilizing the trimeric spike structure, a mechanism previously observed with other class IV-
340 targeting antibodies (32,35,40). ACE2 binding results in the release of S1 and ultimately viral entry.
341 Here, we observed a structural similarity with comparable hyperextension and rotation of the RBD to
342 accommodate 7F binding, features typically associated with class IV S1 shedding antibodies. However,
343 we did not observe shedding in this instance, likely because of stabilizing mutations to the spike
344 ectodomain to facilitate structural studies (32,35).

345 7F exhibits broad neutralization of SARS-CoV-2, SARS-CoV and SARS-like CoV WIV16 with IC₅₀ values
346 in the nM range, even in its monovalent form. Monovalent nanobodies displaying higher SARS-CoV-2
347 neutralization potency, sometimes in the picomolar range, have been described in literature, such as
348 in [38,40]. However, these nanobodies only neutralize SARS-CoV-2 and therefore present a lower
349 neutralization breadth compared to 7F. Additionally, potent broad neutralization of sarbecoviruses by
350 other nanobodies has only been achieved after nanobody dimerization, as observed for VHH72 and

351 Fu2 (24,25). Dimerization of 7F resulted in further improved potency of neutralization, with only a
352 small change in binding affinity. Additionally, dimerization restored neutralization against SARS-CoV-
353 2 VOCs, for which neutralization by monovalent 7F was lost with the S371L mutant in Omicron lineages
354 and beyond. Given that S371L is the only mutation detected within the 7F epitope among the VOCs to
355 date, we anticipate the bivalent 7F constructs to remain active against these variants. The
356 neutralization breadth of 7F towards SARS-CoV-2 and other sarbecoviruses is a significant advantage
357 and highlights its therapeutic potential to combat novel emerging sarbecoviruses.

358 The bivalent 7F-7F construct was specifically designed to facilitate the binding of two RBDs within one
359 spike trimer simultaneously. However, it is possible that 7F also facilitates the crosslinking of spike
360 trimers on the same or different viral particles (intra-virion and inter-virion cross-linking of spikes),
361 potentially explaining the observed increase in neutralization potency in the absence of substantial
362 increase in binding affinity. Interestingly, both 7F-7F and 7F-Fc exhibited equivalent potency in all
363 conducted experiments. The option of generating bivalence through an Fc domain could further
364 enhance protection *in vivo* through Fc-mediated antibody effector functions. While the bivalent 7F-7F
365 could have an advantage in distribution *in vivo*, due to its smaller dimensions.

366 The use of HAE cell cultures in our study provides a physiologically relevant model for investigating
367 respiratory infections. Comprising various epithelial cell types, HAE cultures exhibit a phenotypic
368 resemblance to *in vivo* respiratory epithelium (42,43). Our findings highlight the efficacy of 7F in
369 inhibiting viral infection and spread in this 3D human airway epithelial cell model. Even at low
370 concentrations, 7F demonstrated potent neutralization of authentic SARS-CoV-2 infection in the HAE
371 cell model, even surpassing the effectiveness of remdesivir. This promising result not only highlights
372 the importance of using physiological relevant models in *in vitro* testing, but also supports the
373 therapeutic potential of 7F and emphasizes the promise of this nanobody for further *in vivo*
374 exploration.

375 As sarbecoviruses mainly affect the respiratory tracts, intranasal administration of 7F would be
376 preferred. Previous studies have reported successful intranasal administration of genetically fused and
377 Fc fused SARS-CoV-2 targeting nanobodies in mice and hamster models (18,44–46). Additionally,
378 trimer dimer forming nanobody Fu2 showed potent protection of mice following intraperitoneal
379 administration (24). These findings suggest that intranasal delivery of bivalent 7F could be a viable
380 approach.

381 In conclusion, we have identified a broadly neutralizing nanobody, 7F, with anti-sarbecovirus activity.
382 7F was found to target a conserved class IV epitope on the spike RBD of sarbecoviruses, using a binding
383 mechanism that results in the formation of spike trimer-dimers. Functional and structural data reveal

384 the robust efficacy and molecular basis underlying the neutralization activity of 7F. With its potential
385 to effectively combat infections caused by SARS-CoV, SARS-CoV-2, and related SARS-like
386 coronaviruses, 7F emerges as a promising candidate for addressing future outbreaks of emerging and
387 re-emerging sarbecovirus related diseases in humans.

388

389

390 **Materials and methods**

391 **Nanobody selection**

392 Two llamas were immunized with prefusion trimeric spike proteins of multiple betacoronaviruses;
393 OC43, HKU1, MERS-CoV, SARS-CoV-1 and SARS-CoV-2. The animals received five immunizations in
394 total, starting with SARS-CoV-2 spike followed by the other four spike proteins. Serum collected from
395 the animals before and after immunizations was analyzed in ELISA to check for CoV spike reactivity.
396 From blood collected on day 50, two phage display nanobody libraries (204 and 205) were constructed
397 by an external company (QVQ BV). The libraries combined were used as input for nanobody panning
398 to isolate sarbecovirus spike RBD targeting nanobodies. Two consecutive rounds of panning were
399 performed, for the first round 0.5 µg/mL SARS-CoV-2-RBD protein was coated onto a NUNC Maxisorp
400 strip (Thermo Fisher Scientific) at 4°C overnight. Coated wells were washed 3x using Phosphate-
401 Buffered Saline (PBS) supplemented with 0.1% Tween-20 (PBS-T) and blocked using PBS supplemented
402 with 4% w/v skimmed milk powder (PBSM-4%; Merck Millipore) for 1h at room temperature (RT).
403 Antigen bound phages were eluted using 100 mM TEA buffer pH 12 and subsequently neutralized
404 using 1M Tris-HCl pH 7.5. Eluted phages were amplified in exponentially growing *E.coli* TG1 cells which
405 were infected with M13 helper phages. Phages were purified by a precipitation step using PEG-8000
406 and NaCl, and used as input for a second round of panning on 5 µg/mL SARS-CoV-2 RBD protein.
407 Enrichment after selection was evaluated by titrating infected bacteria on Lysogeny broth (LB) agar
408 plates containing 2% glucose and 100 µg/ml Ampicillin (amp). The output was tested in phage ELISA
409 and periplasmic based ELISA. Promising clones, demonstrating binding to SARS-CoV-2 and SARS-CoV-
410 1 S, were sequenced, and unique sequences of nanobodies were produced and tested again in ELISA
411 for target specificity before being cloned into the pET21a expression vector.

412 **Constructing dimeric nanobodies**

413 To obtain bivalent nanobody 7F-Fc, monovalent nanobody 7F was cloned into a pCG2 plasmid
414 containing the human Fc-domain, using in-fusion cloning. PCR products were generated with
415 overlapping primers (ordered from IDT) for the backbone and insert. Agarose gel electrophoresis was
416 used to separate the backbone and the insert from each other, the appropriate bands were cut out
417 and purified according to gel purification kit protocol (NucleoSpin). A 1:5 ligation, of purified backbone
418 and insert, was performed using NEBuilder® HiFi DNA Assembly Master Mix (New England Biolabs).
419 The ligation product was transformed into DH10B *E.coli* bacteria by heat shock. Success of the
420 molecular cloning was confirmed with Sanger Sequencing performed by Macrogen Europe. The
421 bivalent nanobody, 7F-7F, was constructed through the genetic fusion of two monovalent nanobody
422 sequences connected by a 10 AA glycine serine linker.

423 **Production of nanobodies**

424 Both monovalent 7F and bivalent 7F-7F were produced from a pET21a vector in *E.coli* BL21-DE3 cells.
425 The culture was grown until OD₆₀₀ of ~1 after which cells were induced with 1 mM Isopropyl β-D-1-
426 thiogalactopyranoside (IPTG). After induction, temperature was reduced from 25°C and the culture
427 was incubated overnight. Nanobodies were retrieved from the periplasm by performing two freeze
428 thaw steps and were purified via HisTrap HP columns (Thermo Fisher Scientific) and subsequent size-
429 exclusion chromatography using the superdex 75 10/300 GL column (Cytiva) on the ÄKTAXpress
430 chromatography system.

431 7F-Fc was expressed in Freestyle HEK293-F cells. Transfection of the plasmids into HEK293F was
432 performed using polyethyleneimine (PEI) diluted in Opti-MEM (Gibco). After 24 hours, 300 mM
433 Valporic acid (Sigma-Aldrich) and 10% primateone peptone (Sigma-Aldrich) was added to the
434 transfected cells, which were then incubated until proteins could be harvested. Collected supernatant
435 containing the Fc fused nanobody was incubated overnight with protein-A Sepharose beads (GE
436 Healthcare), after which proteins were purified using poly-prep chromatography columns (Bio-Rad).
437 Bivalent Fc nanobodies were eluted with 0,1 M citric acid (Sigma Aldrich) at pH 2,7. After elution, 3 M
438 Tris-HCl (Sigma Aldrich) at pH 8,8 was added to neutralize the acidic elution. Nanobody concentrations
439 were quantified by absorbance using the NanoDrop (Thermo Fisher Scientific). The purity of the
440 nanobodies was determined by SDS-PAGE and Tris-Glycine gels.

441

442 **Cells**

443 A549 cells (*Homo sapiens*, lung carcinoma, ATCC CCL-185) expressing human ACE2 receptor protein
444 and TMPRSS2 activating protease (A549^{ACE2+TMPRSS2+}) (47) and African green monkey kidney (VeroE6)
445 cells were maintained in Dulbecco's modified Eagle's medium (DMEM) supplemented with 10% FBS,
446 1 mM sodium pyruvate (Gibco), nonessential amino acids (Lonza), penicillin (100 IU/ml), and
447 streptomycin (100 IU/ml). A549^{ACE2+TMPRSS2+} cells were supplemented with blasticidin S (10 µg/mL
448 Gibco) and puromycin (0.5 µg/mL; Thermo Fisher Scientific) to maintain the expression of ACE2 and
449 TMPRSS2 in the cells. Cells were cultured at 37°C in a humidified CO₂ incubator. Cell lines tested
450 negative for mycoplasma.

451 Human airway epithelial (HAE) cells were purchased commercially or isolated from conductive airways
452 resected from transplant patients. The study was approved by the bioethical committee of the Medical
453 University of Silesia in Katowice, Poland (approval no KNW/0022/KB1/17/10, dated 16 February 2010).
454 Written consent was obtained from all patients. All experiments were performed in accordance with

455 relevant guidelines and regulations. In brief, cells were mechanically detached from the tissue after
456 protease treatment. Subsequently, cells were transferred onto permeable Transwell insert supports
457 ($\phi = 6.5$ mm) and cultured in bronchial epithelial growth medium (BEGM). After the cells reached full
458 confluence, the apical medium was removed, and the basolateral medium was replaced with air-liquid
459 interface (ALI) medium. Cells were cultured for 4-6 weeks to form fully differentiated, pseudostratified
460 mucociliary epithelium as previously described (48,49).

461

462 **Viruses**

463 Human codon-optimized genes, which encode the spike proteins of SARS-CoV, SARS-like CoV WIV16,
464 and SARS-CoV-2 (Wuhan, Omicron BA.2, BA.5), were synthesized by GenScript. The generation of the
465 variety of pseudo-typed VSVs followed earlier described procedures (50). In brief, HEK-293T cells were
466 transfected with pCAGGS expression vectors containing the different spike proteins, each with a C-
467 terminal cytoplasmic tail truncated by 28, 18 or 19 residues (SARS-CoV, SARS-CoV-2 and SARS-like
468 WIV16 respectively) to enhance cell surface expression. Subsequently, cells were infected with VSV G-
469 pseudo-typed VSVΔG carrying the firefly luciferase reporter gene 48 hours post-transfection. After 24
470 hours, the supernatant was collected, filtered, and the pseudo-typed VSVs were titrated on VeroE6
471 cells.

472 The SARS-CoV-2 live virus strains used in the study was the SARS-CoV-2 clinical isolate PL1455, which
473 was isolated in-house (hCoV-19/Poland/PL_P18/2020, GISAID accession number: EPI_ISL_451979).
474 Viral stocks were generated by infecting monolayers of VeroE6 cells (ATCC CCL-81). The cytopathic
475 effect was evaluated after 3 days of infection and the cell supernatants were collected, aliquoted, and
476 stored at -80°C . Control samples from mock-infected (noninfected) cells were prepared in the same
477 manner. Virus yield (TCID50/ml) was assessed by titration on confluent A549^{ACE2+TMPRSS2+} using the
478 Reed and Muench method (51).

479

480 **Expression and purification of spike proteins**

481 Trimeric recombinant spike proteins of SARS-CoV-2 and SARS-CoV, and RBD protein of SARS-like CoV
482 WIV16 were expressed and purified as described previously (52). In short, coronavirus spike
483 ectodomain protein of SARS-CoV-2 was expressed transiently in HEK-293T cells with a C-terminal
484 trimerization motif and Strep-tag using the pCAGGS expression plasmid. Similarly, a pCAGGS
485 expression vector encoding RBD protein of SARS-like CoV WIV16 C-terminally tagged with a strep-tag
486 was expressed in HEK-293T. Coronavirus spike ectodomain of SARS-CoV fused with a C-terminal

487 trimerization motif, a thrombin cleavage site and a strep-tag purification tag were in-frame cloned
488 into pMT\Bip\V5\His expression vector. The protein was expressed in HEK-293T. All recombinant
489 proteins were affinity purified from the culture supernatant by streptactin beads (IBA) purification.
490 Purity and integrity of all purified recombinant proteins was checked by Coomassie stained SDS-PAGE.

491

492 **ELISA analysis of nanobody binding to CoV antigens**

493 Nanobodies were tested for binding to recombinant SARS-CoV-2 and SARS-CoV spike protein and to
494 SARS-like CoV WIV-16 RBD protein. 100 ng of protein per well was coated overnight at 4°C onto 96-
495 well NUNC MaxiSorp plates (Thermo Fisher Scientific). Coated plates were washed 3x using PBS and
496 subsequently blocked using PBS supplemented with 2% bovine serum albumin (BSA; Fitzgerald) for 1
497 hour at RT. Nanobodies were allowed to bind to antigen coated plates at tenfold serial dilutions,
498 starting from 5 μ M diluted in 2% BSA PBS, at RT for 2 hour. Nanobody binding to spike was detected
499 using 1:2000 rabbit anti-VHH (QVQ BV) for 1 hour RT followed by 1:2000 IRDye800 conjugated goat-
500 anti-rabbit antibody (Li-COR Biosciences) or 1:1000 goat-anti-rabbit HRPO (Bio-Rad) for 1 hour at RT.
501 Read-out of the IRDye800 secondary antibody, in mean fluorescence intensity 800 (MFI 800), was
502 performed on an Odyssey near-infrared scanner (Li-COR Biosciences). HRP activity was measured at
503 OD 450 nm using tetramethylbenzidine substrate (BioFX) using the BioSPX 800 TS Microplate reader
504 (Tecan). In both cases, apparent binding affinity, K_D , values were calculated by one-site specific non-
505 linear regression on the binding curves (GraphPad Prism version 8.0.2).

506

507 **Biolayer interferometry**

508 Binding analysis was performed using biolayer interferometry on the Octet (ForteBio) at 25°C. All
509 reagents were diluted in PBS. First, 7F (5 μ M) was immobilized onto Ni-NTA biosensors (ForteBio) for
510 20 min. After a brief washing step, antigen binding was performed by incubating the biosensor with 5
511 μ g of recombinant SARS-CoV-2 RBD or NTD protein for 30 min. Data was analyzed using Octet Data
512 Analysis 9.0 (FortéBio).

513

514 **ELISA based Receptor-binding inhibition assay**

515 Recombinant ACE2 protein was coated on 96-well NUNC Maxisorp plates (Thermo Fisher Scientific) at
516 100 ng per well overnight at 4°C. Plates were washed 3x using PBS containing 0.05% Tween-20 and
517 blocked with PBSM-5% for 1 hour at RT. Recombinant strep-tagged SARS-CoV-2 spike or RBD protein

518 (5 nM) was incubated with 4 fold serial diluted antibody or nanobody, starting from 20 nM or 2 μ M
519 respectively, at RT for 2 hours. The starting concentration for the antibodies used was based on their
520 known activity range within this assay. After incubation, the mixture was added to the ACE2 coated
521 plates and incubated for 2 hours at 4°C. Binding of spike or RBD protein to ACE2 was detected using
522 1:2000 HRP-conjugated anti-StrepMAb (IBA). HRP activity was measured at 450 nm using
523 tetramethylbenzidine substrate (BioFX) and an ELISA plate reader (EL-808, BioTek).

524

525 **Pseudotyped virus neutralization assay**

526 Nanobody neutralization was tested against the pseudotyped VSVs. Four-fold serial diluted
527 nanobodies were preincubated with an equal volume of pseudotyped VSV at RT for 1 hour and then
528 inoculated on confluently grown VeroE6 cells. After a 20 hour incubation at 37°C and 5% CO₂, cells
529 were washed once with PBS and subsequently lysed using Passive lysis buffer (Promega). The
530 expression of firefly luciferase was measured on a Berthold Centro LB 960 plate luminometer using d-
531 luciferin as a substrate (Promega). The percentage of neutralization was calculated as the ratio of the
532 reduction in luciferase readout in the presence of nanobody normalized to luciferase readout in the
533 absence of nanobody. Half-maximal inhibitory concentrations (IC₅₀) values were determined using
534 four-parameter logistic regression (GraphPad Prism 8.0.2.).

535

536 **Live virus neutralization assay**

537 Serial nanobody dilutions were mixed with SARS-CoV-2 (1:1 v/v), incubated for 30 min at RT, and
538 overlaid on confluent A549<sup>ACE2+TMPRSS2⁺ cells in a 96-well plate. The final virus titer was 1600 TCID₅₀/ml.
539 The cells were then incubated for 2 hours at 37°C in an atmosphere containing 5% CO₂. The virus-
540 infected cells in the absence of nanobodies were used as a positive control and mock-infected cells
541 were considered a negative control. Remdesivir (10 μ M; Gilead Sciences) was used as a reference. The
542 unbound virus-nanobody complexes were removed by washing them twice with PBS, and nanobodies
543 were reapplied on the cells. Cell culture supernatants were collected 3 days post-infection (p.i.) for
544 RT-qPCR analysis. Experiments were carried out three times with each sample tested in duplicate.</sup>

545 HAE cultures were apically infected with a mixture of SARS-CoV-2 PL1455 and nanobodies similarly to
546 the A549<sup>ACE2+TMPRSS2⁺ cells. After incubation and washing the cultures, nanobodies were administered
547 to the apical side of the inserts, incubated for 15 min at 37°C and samples were collected for RT-qPCR
548 analysis. The administration and collection of the samples were repeated every 24 hours until 72 h p.i.
549 Experiments in HAE cultures were performed twice with each sample tested in duplicate.</sup>

550 The isolation of viral RNA from cell culture supernatants was performed automatically using the
551 MagnifiQ 96 Pathogen instant kit (A&A Biotechnology) and the KingFisher Flex System (Thermo Fisher
552 Scientific) according to the manufacturer's protocol. Subsequently, viral RNA was reverse transcribed
553 and quantified using GoTaq Probe 1-Step RT-qPCR System kit (Promega) in the presence of the specific
554 SARS-CoV-2 probe (5'-6-FAM-ACT TCC TCA AGG AAC AAC ATT GCC A-BHQ-1-3'; 200 nM) and primers
555 (Forward: 5'-CAC ATT GGC ACC CGC AAT C-3', 600 nM; Reverse: 5'-GAG GAA CGA GAA GAG GCT TG-
556 3', 800 nM). Appropriate standards for the N gene of the virus were prepared to evaluate the number
557 of viral RNA molecules in the samples. The reaction was performed in a thermal cycler (CFX Touch
558 Real-Time PCR Detection System, Bio-Rad) with the heating scheme as follows: 15 min at 45°C, 2 min
559 at 95°C, 40 cycles of 15 s at 95°C and 1 min at 56°C.

560

561 **Cryo-electron microscopy sample preparation and data collection**

562 For the spike-7F complex, 2.5 μ l 6P stabilized SARS-CoV-2 S-ectodomain, at a concentration of 28 μ M
563 (based on the molecular weight of the spike protomer) was combined with 0.1 μ l of 140 μ M 7F and
564 incubated for \sim 15 min at room temperature. Immediately before blotting and plunge freezing, 0.5 μ l
565 of 0.1% (w/v) fluorinated octyl maltoside (FOM) was added to the sample, resulting in a final FOM
566 concentration of 0.01% (w/v). The sample solution (3 μ l) was applied to glow-discharged (20 mAmp,
567 30 sec, Quorum GloQube) Quantifoil R1.2/1.3 grids (Quantifoil Micro Tools GmbH), blotted for 5 s
568 using blot force 0 and plunge frozen into liquid ethane using Vitrobot Mark IV (Thermo Fisher
569 Scientific). The data were collected on a Thermo Scientific™ Krios™ G4 Cryo Transmission Electron
570 Microscope (Cryo-TEM) equipped with Selectris X Imaging Filter (Thermo Fisher Scientific) and Falcon
571 4i Direct Electron Detector (Thermo Fisher Scientific) operated in Electron-Event representation (EER)
572 mode. In total, 1,948 movies were collected at a nominal magnification of 165,000 \times , corresponding to
573 a calibrated pixel size of 0.73 \AA /pix over a defocus range of -0.75 to -1.5 μ m. A full list of data collection
574 parameters can be found in Table S2.

575

576 **Single particle image processing**

577 Data processing was performed using the CryoSPARC Software package (53). After patch-motion and
578 CTF correction, particles were picked using a blob picker, extracted 4x binned and subjected to 2D
579 classification. Following 2D classification, particles belonging to class averages that displayed high-
580 resolution detail were selected for ab-initio reconstruction into six classes. Particles belonging to the
581 spike trimer dimer complex classes were re-extracted 1.5x binned, resulting in a pixel size of 2.19 \AA .

582 The spike-7F particles were subjected to non-uniform refinement with D3 symmetry (54). At this point,
583 the global resolution of the complex was 3.3 Å, however, the interfaces between spike and nanobody
584 was resolved to a lower resolution. To improve the local resolution, particles in the final D3 global
585 reconstruction were symmetry expanded, a custom mask encompassing one RBD and one nanobody
586 involved in the head-to-head spike trimer dimer formation was used to carry out a cryoSPARC local
587 refinement (BETA). This markedly improved local resolution, with the epitope resolved to a resolution
588 of 3.1 Å, enabling sufficient confidence for modelling this epitope-paratope regions. For a more
589 detailed processing methodology, see Fig.S2 and Fig.S3.

590

591 **Model building and refinement**

592 UCSF Chimera (55) (version 1.15.0) and Coot (56) (version 0.9.6) were used for model building. The
593 structure of the SARS-CoV-2 spike glycoprotein previously resolved (PDB ID 7R40) (57) and AlphaFold2
594 generated 7F nanobody (58,59) was used as a starting point for modelling of the spike-7F complex.
595 Models were individually rigid body fitted into the density map using the UCSF Chimera “Fit in map”
596 tool and then combined. The resulting model was then edited in Coot using the ‘real-space refinement’,
597 carbohydrate module (60) and ‘sphere refinement’ tool. To improve fitting, Namdinator (61) was
598 utilised, using molecular dynamics flexible fitting of all models. Following this, iterative rounds of
599 manual fitting in Coot and real space refinement in Phenix (62) were carried out to improve rotamer,
600 bond angle and Ramachandran outliers. During refinement with Phenix, secondary structure and non-
601 crystallographic symmetry restraints were imposed. The final model was validated in Phenix with
602 MolProbity (63), EMRinger (64) and fitted glycans validated using Privateer (65,66).

603

604 **Structure analysis and visualization**

605 Interacting residues of SARS-CoV-2 spike-7F epitopes were identified using PDBePISA (67) and LigPlot+
606 (68). Figures were generated using UCSF ChimeraX (69). Structural biology applications used in this
607 project were compiled and configured by SBGrid (70).

608

609 **References**

- 610 1. Zhong NS, Zheng BJ, Li YM, Poon null, Xie ZH, Chan KH, et al. Epidemiology and cause of severe
611 acute respiratory syndrome (SARS) in Guangdong, People's Republic of China, in February, 2003.
612 *Lancet.* 2003 Oct 25;362(9393):1353–8.
- 613 2. Zhou P, Yang XL, Wang XG, Hu B, Zhang L, Zhang W, et al. A pneumonia outbreak associated with
614 a new coronavirus of probable bat origin. *Nature.* 2020 Mar;579(7798):270–3.
- 615 3. Lu R, Zhao X, Li J, Niu P, Yang B, Wu H, et al. Genomic characterisation and epidemiology of 2019
616 novel coronavirus: implications for virus origins and receptor binding. *The Lancet.* 2020 Feb
617 22;395(10224):565–74.
- 618 4. Ge XY, Li JL, Yang XL, Chmura AA, Zhu G, Epstein JH, et al. Isolation and characterization of a bat
619 SARS-like coronavirus that uses the ACE2 receptor. *Nature.* 2013 Nov;503(7477):535–8.
- 620 5. Li W, Moore MJ, Vasilieva N, Sui J, Wong SK, Berne MA, et al. Angiotensin-converting enzyme 2
621 is a functional receptor for the SARS coronavirus. *Nature.* 2003 Nov 27;426(6965):450–4.
- 622 6. Wang Q, Zhang Y, Wu L, Niu S, Song C, Zhang Z, et al. Structural and Functional Basis of SARS-
623 CoV-2 Entry by Using Human ACE2. *Cell.* 2020 May 14;181(4):894-904.e9.
- 624 7. Wrapp D, Wang N, Corbett KS, Goldsmith JA, Hsieh CL, Abiona O, et al. Cryo-EM structure of the
625 2019-nCoV spike in the prefusion conformation. *Science.* 2020 Mar 13;367(6483):1260–3.
- 626 8. Benton DJ, Wrobel AG, Xu P, Roustan C, Martin SR, Rosenthal PB, et al. Receptor binding and
627 priming of the spike protein of SARS-CoV-2 for membrane fusion. *Nature.* 2020
628 Dec;588(7837):327–30.
- 629 9. Almagro JC, Mellado-Sánchez G, Pedraza-Escalona M, Pérez-Tapia SM. Evolution of Anti-SARS-
630 CoV-2 Therapeutic Antibodies. *Int J Mol Sci.* 2022 Aug 28;23(17):9763.
- 631 10. Arbab Ghahroudi M, Desmyter A, Wyns L, Hamers R, Muyldermans S. Selection and
632 identification of single domain antibody fragments from camel heavy-chain antibodies. *FEBS
633 Letters.* 1997;414(3):521–6.
- 634 11. Greenberg AS, Avila D, Hughes M, Hughes A, McKinney EC, Flajnik MF. A new antigen receptor
635 gene family that undergoes rearrangement and extensive somatic diversification in sharks.
636 *Nature.* 1995 Mar 9;374(6518):168–73.
- 637 12. Hamers-Casterman C, Atarhouch T, Muyldermans S, Robinson G, Hammers C, Songa EB, et al.
638 Naturally occurring antibodies devoid of light chains. *Nature.* 1993 Jun;363(6428):446–8.
- 639 13. Vu KB, Ghahroudi MA, Wyns L, Muyldermans S. Comparison of llama VH sequences from
640 conventional and heavy chain antibodies. *Mol Immunol.* 1997;34(16–17):1121–31.
- 641 14. Kunz P, Zinner K, Mücke N, Bartoschik T, Muyldermans S, Hoheisel JD. The structural basis of
642 nanobody unfolding reversibility and thermostability. *Sci Rep.* 2018 May 21;8(1):7934.
- 643 15. Swart IC, Van Gelder W, De Haan CAM, Bosch BJ, Oliveira S. Next generation single-domain
644 antibodies against respiratory zoonotic RNA viruses. *Front Mol Biosci.* 2024 May 9;11.

645 16. Van Heeke G, Allosery K, De Brabandere V, De Smedt T, Detalle L, de Fougerolles A.
646 Nanobodies®††Nanobody is a registered trademark of Ablynx NV. as inhaled biotherapeutics for
647 lung diseases. *Pharmacology & Therapeutics*. 2017 Jan 1;169:47–56.

648 17. Fortuna A, Alves G, Serralheiro A, Sousa J, Falcão A. Intranasal delivery of systemic-acting drugs:
649 Small-molecules and biomacromolecules. *European Journal of Pharmaceutics and*
650 *Biopharmaceutics*. 2014 Sep 1;88(1):8–27.

651 18. Liu H, Wu L, Liu B, Xu K, Lei W, Deng J, et al. Two pan-SARS-CoV-2 nanobodies and their
652 multivalent derivatives effectively prevent Omicron infections in mice. *Cell Reports Medicine*.
653 2023 Feb;4(2):100918.

654 19. Xiang Y, Huang W, Liu H, Sang Z, Nambulli S, Tubiana J, et al. Superimmunity by pan-sarbecovirus
655 nanobodies. *Cell Reports*. 2022 Jun 28;39(13):111004.

656 20. Li M, Ren Y, Aw ZQ, Chen B, Yang Z, Lei Y, et al. Broadly neutralizing and protective nanobodies
657 against SARS-CoV-2 Omicron subvariants BA.1, BA.2, and BA.4/5 and diverse sarbecoviruses. *Nat*
658 *Commun*. 2022 Dec 27;13(1):7957.

659 21. Chen WH, Hajduczki A, Martinez EJ, Bai H, Matz H, Hill TM, et al. Shark nanobodies with potent
660 SARS-CoV-2 neutralizing activity and broad sarbecovirus reactivity. *Nat Commun*. 2023 Feb
661 3;14(1):580.

662 22. Yang X, Duan H, Liu X, Zhang X, Pan S, Zhang F, et al. Broad Sarbecovirus Neutralizing Antibodies
663 Obtained by Computational Design and Synthetic Library Screening. *Journal of Virology*. 2023
664 Jun 27;97(7):e00610-23.

665 23. Hollingsworth SA, Noland CL, Vroom K, Saha A, Sam M, Gao Q, et al. Discovery and
666 multimerization of cross-reactive single-domain antibodies against SARS-like viruses to enhance
667 potency and address emerging SARS-CoV-2 variants. *Sci Rep*. 2023 Aug 22;13:13668.

668 24. Hanke L, Das H, Sheward DJ, Perez Vidakovics L, Urgard E, Moliner-Morro A, et al. A bispecific
669 monomeric nanobody induces spike trimer dimers and neutralizes SARS-CoV-2 in vivo. *Nat*
670 *Commun*. 2022 Jan 10;13:155.

671 25. Wrapp D, De Vlieger D, Corbett KS, Torres GM, Wang N, Van Breedam W, et al. Structural Basis
672 for Potent Neutralization of Betacoronaviruses by Single-Domain Camelid Antibodies. *Cell*. 2020
673 May 28;181(5):1004-1015.e15.

674 26. Chen Y, Zhao X, Zhou H, Zhu H, Jiang S, Wang P. Broadly neutralizing antibodies to SARS-CoV-2
675 and other human coronaviruses. *Nat Rev Immunol*. 2023 Mar;23(3):189–99.

676 27. Pinto D, Park YJ, Beltramello M, Walls AC, Tortorici MA, Bianchi S, et al. Cross-neutralization of
677 SARS-CoV-2 by a human monoclonal SARS-CoV antibody. *Nature*. 2020 Jul;583(7815):290–5.

678 28. Barnes CO, Jette CA, Abernathy ME, Dam KMA, Esswein SR, Gristick HB, et al. SARS-CoV-2
679 neutralizing antibody structures inform therapeutic strategies. *Nature*. 2020
680 Dec;588(7839):682–7.

681 29. Yuan M, Wu NC, Zhu X, Lee CCD, So RTY, Lv H, et al. A highly conserved cryptic epitope in the
682 receptor binding domains of SARS-CoV-2 and SARS-CoV. *Science (New York, N.Y.)*. 2020 May
683 5;368(6491):630.

684 30. Tortorici MA, Czudnochowski N, Starr TN, Marzi R, Walls AC, Zatta F, et al. Broad sarbecovirus
685 neutralization by a human monoclonal antibody. *Nature*. 2021 Sep;597(7874):103–8.

686 31. Piccoli L, Park YJ, Tortorici MA, Czudnochowski N, Walls AC, Beltramello M, et al. Mapping
687 Neutralizing and Immunodominant Sites on the SARS-CoV-2 Spike Receptor-Binding Domain by
688 Structure-Guided High-Resolution Serology. *Cell*. 2020 Nov 12;183(4):1024-1042.e21.

689 32. Zhou D, Duyvesteyn HME, Chen CP, Huang CG, Chen TH, Shih SR, et al. Structural basis for the
690 neutralization of SARS-CoV-2 by an antibody from a convalescent patient. *Nat Struct Mol Biol*.
691 2020 Oct;27(10):950–8.

692 33. Lv Z, Deng YQ, Ye Q, Cao L, Sun CY, Fan C, et al. Structural basis for neutralization of SARS-CoV-2
693 and SARS-CoV by a potent therapeutic antibody. *Science*. 2020 Sep 18;369(6510):1505–9.

694 34. Wang Y, Zhan W, Liu J, Wang Y, Zhang X, Zhang M, et al. A broadly neutralizing antibody against
695 SARS-CoV-2 Omicron variant infection exhibiting a novel trimer dimer conformation in spike
696 protein binding. *Cell Res*. 2022 Sep;32(9):862–5.

697 35. Huo J, Zhao Y, Ren J, Zhou D, Duyvesteyn HME, Ginn HM, et al. Neutralization of SARS-CoV-2 by
698 Destruction of the Prefusion Spike. *Cell Host & Microbe*. 2020 Sep 9;28(3):445-454.e6.

699 36. Hsieh CL, Goldsmith JA, Schaub JM, DiVenere AM, Kuo HC, Javanmardi K, et al. Structure-based
700 design of prefusion-stabilized SARS-CoV-2 spikes. *Science*. 2020 Sep 18;369(6510):1501–5.

701 37. Shang J, Ye G, Shi K, Wan Y, Luo C, Aihara H, et al. Structural basis of receptor recognition by
702 SARS-CoV-2. *Nature*. 2020 May;581(7807):221–4.

703 38. Saville JW, Mannar D, Zhu X, Srivastava SS, Berezuk AM, Demers JP, et al. Structural and
704 biochemical rationale for enhanced spike protein fitness in delta and kappa SARS-CoV-2
705 variants. *Nat Commun*. 2022 Feb 8;13(1):742.

706 39. Xu J, Xu K, Jung S, Conte A, Lieberman J, Muecksch F, et al. Nanobodies from camelid mice and
707 llamas neutralize SARS-CoV-2 variants. *Nature*. 2021 Jul;595(7866):278–82.

708 40. Huo J, Mikolajek H, Le Bas A, Clark JJ, Sharma P, Kipar A, et al. A potent SARS-CoV-2 neutralising
709 nanobody shows therapeutic efficacy in the Syrian golden hamster model of COVID-19. *Nat
710 Commun*. 2021 Sep 22;12(1):5469.

711 41. Gütter T, Aksu M, Dickmanns A, Stegmann KM, Gregor K, Rees R, et al. Neutralization of SARS-
712 CoV-2 by highly potent, hyperthermostable, and mutation-tolerant nanobodies. *EMBO J*. 2021
713 Oct 1;40(19):e107985.

714 42. Gray TE, Guzman K, Davis CW, Abdullah LH, Nettesheim P. Mucociliary differentiation of serially
715 passaged normal human tracheobronchial epithelial cells. *Am J Respir Cell Mol Biol*. 1996
716 Jan;14(1):104–12.

717 43. Dvorak A, Tilley AE, Shaykhiev R, Wang R, Crystal RG. Do airway epithelium air-liquid cultures
718 represent the in vivo airway epithelium transcriptome? *Am J Respir Cell Mol Biol*. 2011
719 Apr;44(4):465–73.

720 44. Titong A, Gallolu Kankamalage S, Dong J, Huang B, Spadoni N, Wang B, et al. First-in-class
721 trispecific VHH-Fc based antibody with potent prophylactic and therapeutic efficacy against
722 SARS-CoV-2 and variants. *Sci Rep*. 2022 Mar 9;12(1):4163.

723 45. Ma H, Zhang X, Zeng W, Zhou J, Chi X, Chen S, et al. A bispecific nanobody dimer broadly
724 neutralizes SARS-CoV-1 & 2 variants of concern and offers substantial protection against
725 Omicron via low-dose intranasal administration. *Cell Discov.* 2022 Dec 9;8(1):1–14.

726 46. Wu X, Cheng L, Fu M, Huang B, Zhu L, Xu S, et al. A potent bispecific nanobody protects hACE2
727 mice against SARS-CoV-2 infection via intranasal administration. *Cell Rep.* 2021 Oct
728 19;37(3):109869.

729 47. Synowiec A, Jedrysiak M, Branicki W, Klajmon A, Lei J, Owczarek K, et al. Identification of Cellular
730 Factors Required for SARS-CoV-2 Replication. *Cells.* 2021 Nov 13;10(11):3159.

731 48. Milewska A, Kula-Pacurar A, Wadas J, Suder A, Szczepanski A, Dabrowska A, et al. Replication of
732 Severe Acute Respiratory Syndrome Coronavirus 2 in Human Respiratory Epithelium. *J Virol.*
733 2020 Jul 16;94(15):e00957-20.

734 49. Barreto-Duran E, Szczepański A, Gałuszka-Bulaga A, Surmiak M, Siedlar M, Sanak M, et al. The
735 interplay between the airway epithelium and tissue macrophages during the SARS-CoV-2
736 infection. *Front Immunol.* 2022 Oct 6;13:991991.

737 50. Wang C, Li W, Drabek D, Okba NMA, van Haperen R, Osterhaus ADME, et al. A human
738 monoclonal antibody blocking SARS-CoV-2 infection. *Nat Commun.* 2020 May 4;11(1):2251.

739 51. Determination of 50% endpoint titer using a simple formula - PMC [Internet]. [cited 2024 Mar
740 1]. Available from: <https://www.ncbi.nlm.nih.gov/pmc/articles/PMC4861875/>

741 52. Fedry J, Hurdiss DL, Wang C, Li W, Obal G, Drulyte I, et al. Structural insights into the cross-
742 neutralization of SARS-CoV and SARS-CoV-2 by the human monoclonal antibody 47D11. *Science
743 Advances.* 2021 Jun 2;7(23):eabf5632.

744 53. Punjani A, Rubinstein JL, Fleet DJ, Brubaker MA. cryoSPARC: algorithms for rapid unsupervised
745 cryo-EM structure determination. *Nat Methods.* 2017 Mar;14(3):290–6.

746 54. Punjani A, Zhang H, Fleet DJ. Non-uniform refinement: adaptive regularization improves single-
747 particle cryo-EM reconstruction. *Nat Methods.* 2020 Dec;17(12):1214–21.

748 55. Pettersen EF, Goddard TD, Huang CC, Couch GS, Greenblatt DM, Meng EC, et al. UCSF Chimera--
749 a visualization system for exploratory research and analysis. *J Comput Chem.* 2004
750 Oct;25(13):1605–12.

751 56. Emsley P, Cowtan K. Coot: model-building tools for molecular graphics. *Acta Crystallogr D Biol
752 Crystallogr.* 2004 Dec;60(Pt 12 Pt 1):2126–32.

753 57. Du W, Hurdiss DL, Drabek D, Mykytyn AZ, Kaiser FK, González-Hernández M, et al. An ACE2-
754 blocking antibody confers broad neutralization and protection against Omicron and other SARS-
755 CoV-2 variants of concern. *Science Immunology.* 2022 Apr 26;7(73):eabp9312.

756 58. Tunyasuvunakool K, Adler J, Wu Z, Green T, Zielinski M, Žídek A, et al. Highly accurate protein
757 structure prediction for the human proteome. *Nature.* 2021 Aug;596(7873):590–6.

758 59. Mirdita M, Schütze K, Moriwaki Y, Heo L, Ovchinnikov S, Steinegger M. ColabFold: making
759 protein folding accessible to all. *Nat Methods.* 2022 Jun;19(6):679–82.

760 60. Emsley P, Crispin M. Structural analysis of glycoproteins: building N-linked glycans with Coot.
761 *Acta Crystallogr D Struct Biol.* 2018 Apr 6;74(Pt 4):256–63.

762 61. Kidmose RT, Juhl J, Nissen P, Boesen T, Karlsen JL, Pedersen BP. Namdinator - automatic
763 molecular dynamics flexible fitting of structural models into cryo-EM and crystallography
764 experimental maps. *IUCrJ.* 2019 Jul 1;6(Pt 4):526–31.

765 62. Headd JJ, Echols N, Afonine PV, Grosse-Kunstleve RW, Chen VB, Moriarty NW, et al. Use of
766 knowledge-based restraints in phenix.refine to improve macromolecular refinement at low
767 resolution. *Acta Crystallogr D Biol Crystallogr.* 2012 Apr;68(Pt 4):381–90.

768 63. Chen VB, Arendall WB, Headd JJ, Keedy DA, Immormino RM, Kapral GJ, et al. MolProbity: all-
769 atom structure validation for macromolecular crystallography. *Acta Crystallogr D Biol
770 Crystallogr.* 2010 Jan;66(Pt 1):12–21.

771 64. Barad BA, Echols N, Wang RYR, Cheng Y, DiMaio F, Adams PD, et al. EMRinger: side chain-
772 directed model and map validation for 3D cryo-electron microscopy. *Nat Methods.* 2015
773 Oct;12(10):943–6.

774 65. Agirre J, Davies G, Wilson K, Cowtan K. Carbohydrate anomalies in the PDB. *Nat Chem Biol.* 2015
775 May;11(5):303.

776 66. Agirre J, Iglesias-Fernández J, Rovira C, Davies GJ, Wilson KS, Cowtan KD. Privateer: software for
777 the conformational validation of carbohydrate structures. *Nat Struct Mol Biol.* 2015
778 Nov;22(11):833–4.

779 67. Krissinel E, Henrick K. Inference of macromolecular assemblies from crystalline state. *J Mol Biol.*
780 2007 Sep 21;372(3):774–97.

781 68. Laskowski RA, Swindells MB. LigPlot+: multiple ligand-protein interaction diagrams for drug
782 discovery. *J Chem Inf Model.* 2011 Oct 24;51(10):2778–86.

783 69. Pettersen EF, Goddard TD, Huang CC, Meng EC, Couch GS, Croll TI, et al. UCSF ChimeraX:
784 Structure visualization for researchers, educators, and developers. *Protein Sci.* 2021
785 Jan;30(1):70–82.

786 70. Morin A, Eisenbraun B, Key J, Sanschagrin PC, Timony MA, Ottaviano M, et al. Collaboration gets
787 the most out of software. *Elife.* 2013 Sep 10;2:e01456.

788

789

790 **Declarations**

791 **Ethics approval and consent to participate**

792 Not applicable

793

794 **Consent for publication**

795 Not applicable

796

797 **Availability of data and materials**

798 All data generated or analyzed during this study are included in this published article [and its
799 supplementary information files]. The cryo-EM maps and atomic structures have been deposited in
800 the Protein Data Bank (PDB) Electron Microscopy Data Bank (EMDB) under accession codes: 9FR3 and
801 EMD-50707 for SARS-CoV-2 S with nanobody-7F (global), and 9FR4 and EMD-50708 for SARS-CoV-2 S
802 with nanobody-7F (local). Source data are provided with this paper.

803

804 **Competing interests**

805 ID is an employee of Thermo Fisher Scientific. The remaining authors declare that they have no
806 competing interests.

807

808 **Funding**

809 This research was partially funded by the research programme of the Netherlands Centre for One
810 Health (www.ncoh.nl).

811 This work was partially funded by the Corona Accelerated R&D in Europe (CARE) project. The CARE
812 project has received funding from the Innovative Medicines Initiative 2 Joint Undertaking (JU) under
813 grant agreement No 101005077. The JU receives support from the European Union's Horizon 2020
814 Research and Innovation Programme, the European Federation of Pharmaceutical Industries and
815 Associations, the Bill & Melinda Gates Foundation, the Global Health Drug Discovery Institute and the
816 University of Dundee. The content of this publication only reflects the author's views, and the JU is
817 not responsible for any use that may be made of the information it contains.

818

819

820

821 **Author Contributions**

822 ICS, OJD, DLH, BJB, SO designed the research project; ICS, OJD, planned and executed experiments; ID
823 cryo-EM grid preparation and data collection; OJD and DLH cryo-EM data processing; OJD model
824 building; TB, MC, MB assisted with experiments; AZ, KP executed and reviewed live virus and HAE
825 culture experiment; ICS, OJD analyzed data and wrote the manuscript; ICS, OJD made the figures; DLH,
826 BJB, SO reviewed data, and reviewed and edited the manuscript; CAMH, SO acquired the funding. All
827 authors reviewed the manuscript.

828

829 **Acknowledgements**

830 Not applicable.